

Complicated Interaction of Dynamic Recrystallization and Precipitation During Hot Deformation of Ultrahigh-Strength Stainless Steel



XIAOHUI WANG, ZHENBAO LIU, and HAIWEN LUO

A new ultrahigh-strength stainless steel was compressed at the temperature range of 1273 K to 1423 K (1000 °C to 1150 °C) with a strain rate varying from 0.01 to 10 s⁻¹ using a thermomechanical simulator. The microstructures quenched after hot deformation were examined. It was found that dynamic recrystallization (DRX) could occur in this heavily alloyed steel during the entire studied deformation condition. In contrast, dynamic precipitation only takes place at temperatures below 1373 K (1100 °C) and its influence on DRX depends on both deformation temperature and strain rate. The critical strain for the onset of DRX increases as usual with the decreasing temperature or the increasing strain rate; however, it decreases with the increase of strain rate from 1 to 10 s⁻¹ at the temperatures of 1273 K and 1323 K (1000 °C and 1050 °C). This is attributed to the complicated interaction of DRX and dynamic precipitation when both can occur during deformation. On the one hand, dynamic precipitation could occur during deformation below 1373 K (1100 °C) and then suppress DRX due to the pinning of migrating boundaries. On the other hand, such a suppression shall decrease when not enough particles could dynamically precipitate during the short period of deformation at a high strain rate, which should facilitate DRX. Therefore, strain rate has a complicated influence on DRX kinetics. Finally, we developed quantitative models, which can successfully predict the critical strain for DRX, the recrystallized fraction, and grain sizes using the Zener–Holloman parameter as a mere input. Moreover, this model can also simulate the unusual acceleration of DRX at the high strain rate, resulting from the above-stated complicated interaction of dynamic precipitation and DRX.

DOI: 10.1007/s11661-016-3743-9

© The Minerals, Metals & Materials Society and ASM International 2016

I. INTRODUCTION

LOW-ALLOYED, ultrahigh-strength steel, such as the well-known 300M steel grade, has been widely used due to its excellent combination of ultrahigh ultimate tensile strength (UTS) of around 1700 MPa and good toughness. Its poor corrosion resistance, however, leads to a remarkably reduced service life in the case of attacking environments. Thus, it has to be coated with cadmium, which is harmful to the environment and shall be banned in the future. Therefore, ultrahigh-strength stainless steel (UHSSS) is then considered to be an alternative for this application^[1,2] because it has a good combination of corrosion resistance, ultrahigh strength, and high toughness. Recently, we have developed a new type of UHSSS containing high contents of Cr, Ni, Co,

and Mo. It exhibits a UTS higher than 1900 MPa, excellent corrosion resistance, and good toughness.^[3,4] Nevertheless, the heavy alloying leads to high resisting force and poor hot plasticity during hot working and, unfortunately, to frequent cracking. Therefore, we have to optimize the hot working process to suppress cracking *via* recrystallization;^[5–7] the latter can restore the hot plasticity of work hardened materials and lead to a significant grain refinement.

Dynamic recrystallization (DRX) often occurs during the hot deformation of stainless steels because they have low stacking fault energy (SFE).^[8–10] DRX is usually characterized by the nucleation and growth of new grains at pre-existing grain boundaries. Figure 1(a) schematically shows typical flow stress–strain curves, resulting from different restoration mechanisms during hot deformation. When dynamic recovery (DRV) operates during deformation, stress first increases due to the work hardening and then approaches to a constant value, σ_{S1} .^[11] When DRX occurs, the flow curve usually exhibits a peak, followed by a lower and steady flow with the proceeding deformation. DRX is initiated at the critical stress, σ_c , which is usually smaller than the peak stress, σ_p . Mirzadeh and Najafzadeh have managed to determine the critical stress for DRX from the curve of strain hardening rate, θ , vs strain.^[12] At the critical stress, the local bulges of grain boundaries grow

XIAOHUI WANG, Ph.D. Student, is with the School of Metallurgical and Ecological Engineering, University of Science and Technology Beijing, 30 Xue Yuan Lu, Beijing 100083, P.R. China, and also Researcher with the Division of Special Steels, Central Iron and Steel Research Institute, 76 Xue yuan Nan Lu, Beijing 100081, P.R. China. ZHENBAO LIU, Senior Engineer, is with the Division of Special Steels, Central Iron and Steel Research Institute. HAIWEN LUO, Professor, is with the School of Metallurgical and Ecological Engineering, University of Science and Technology Beijing. Contact e-mail: luohaiwen@ustb.edu.cn.

Manuscript submitted April 18, 2016.

Article published online October 13, 2016

and occupy the prior boundaries and finally form the so-called “necklace structure” until the peak stress.^[13,14] In particular, Poliak and Jonas^[15] have demonstrated how to determine the critical stress for DRX, σ_c , as the lowest point at the curve of $-d\theta/d\sigma$ vs σ in Figure 1(b). In this article, the influences of both deformation temperature and strain rate on DRX were studied using hot compression tests. Both the critical stress/strain for DRX and microstructures after compression were analyzed with their dependence on temperature and strain rate.

II. EXPERIMENTAL

The chemical compositions of studied UHSSS are 0.2 pct C-13.0 pct Cr-14.0 pct Co-5.0 pct Mo-2.0 pct Ni-2 pct (W + V) in weight percentage. The cylindrical specimen with a diameter of 8 mm and height of 15 mm was isothermally compressed on a thermal-mechanical simulator, Gleeble-3800. It was first heated at 10 K/s (10 °C/s) to 1523 K (1250 °C) and held for 5 minutes for

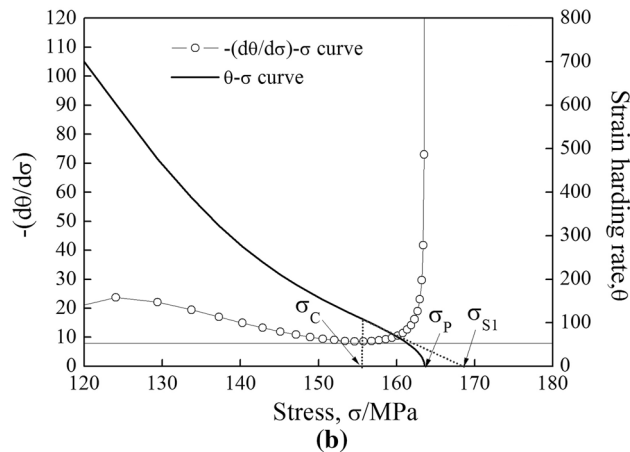
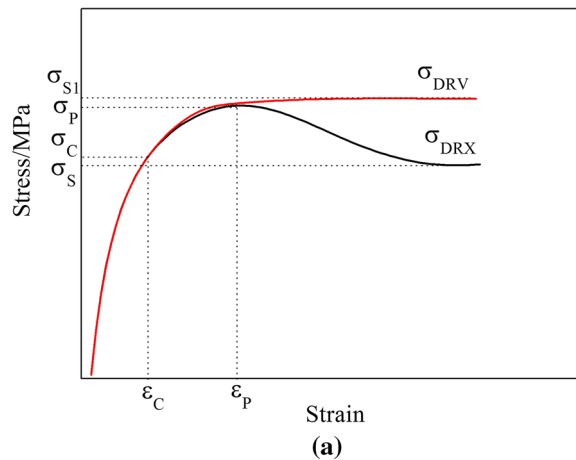


Fig. 1—Typical flow curves under either DRX or DRV (a) and the curves of θ (strain hardening rate) vs σ (flow stress) and $-d\theta/d\sigma$ vs σ (b). σ_c is the critical strain for the onset of DRX and can be determined as the lowest point of $-d\theta/d\sigma$ vs σ curve. σ_{S1} is the saturated stress when dynamic restoration is only due to DRV and determined as the intercept of θ - σ curve at the X axis.

homogenization; next, it was cooled at 10 K/s (10 °C/s) to different test temperatures ranging 1273 K to 1423 K (1000 °C to 1150 °C). After a short isothermal holding for 5 seconds to minimize the thermal gradient, the specimen was compressed to a true strain of 1.0 at the different rates of 0.01, 0.1, 1, and 10 s⁻¹, followed by water quenching. The quenched specimens were sectioned in the middle along the compression direction, on which microstructures were carefully examined *via* both optical and scanning electronic microscopes after the conventional polishing and the etching by the solution of 1-g potassium permanganate plus 10-mL sulfuric acid plus 90-mL ethyl alcohol. Grain sizes were measured using the mean linear intercept method.

III. RESULTS

A. Flow Curves

The stress–strain curves at various temperatures and strain rates are given in Figure 2. All the stress–strain curves exhibit a single peak followed by a steady and lower flow stress, indicating that DRX should occur during all the tests even though both temperature and strain rate vary in such wide ranges.^[16,17] Flow stress increases at both lower temperature and higher strain rate. It is worth mentioning that the flow stress tends to increase again when strain is more than 0.7 during all the tests. We infer that this should result from the significantly increased friction force between the compressed specimen and anvils due to increased contact area above this strain.

B. Microstructural Examination

1. Precipitates

Precipitates at grain boundaries were observed on the samples after deformation at 1273 K and 1323 K (1000 °C and 1050 °C), as shown in Figure 3. Most of them are located at recrystallized grain boundaries with the sizes varying from 100 to 500 nm, suggesting that these migrating boundaries may be inhibited by these particles due to the pinning force. These particles are presumed as M_6C carbide because thermodynamic calculation using ThermoCalc and the database of TCFE7 indicates that only M_6C can precipitate below 1353 K (1080 °C) and is stable at both temperatures as given in Figure 3(f). The EDS measurements (Figure 3(e)) indicate that such M_6C particles contain high contents of Cr, Mo, and Co, which also agrees with the thermodynamic calculation. Moreover, both the quantity and size of precipitates decrease with the increase of strain rate because a higher strain rate leads to shorter time for carbide particles to precipitate and grow. The strain rate has a two-fold influence on dynamic precipitation of carbide particles during deformation. On the one hand, a higher strain rate usually leads to a higher work hardening rate and a larger suppression of DRX, thereby an enhanced nucleation rate of dynamic precipitation as more dislocations are introduced as nucleation sites; on the

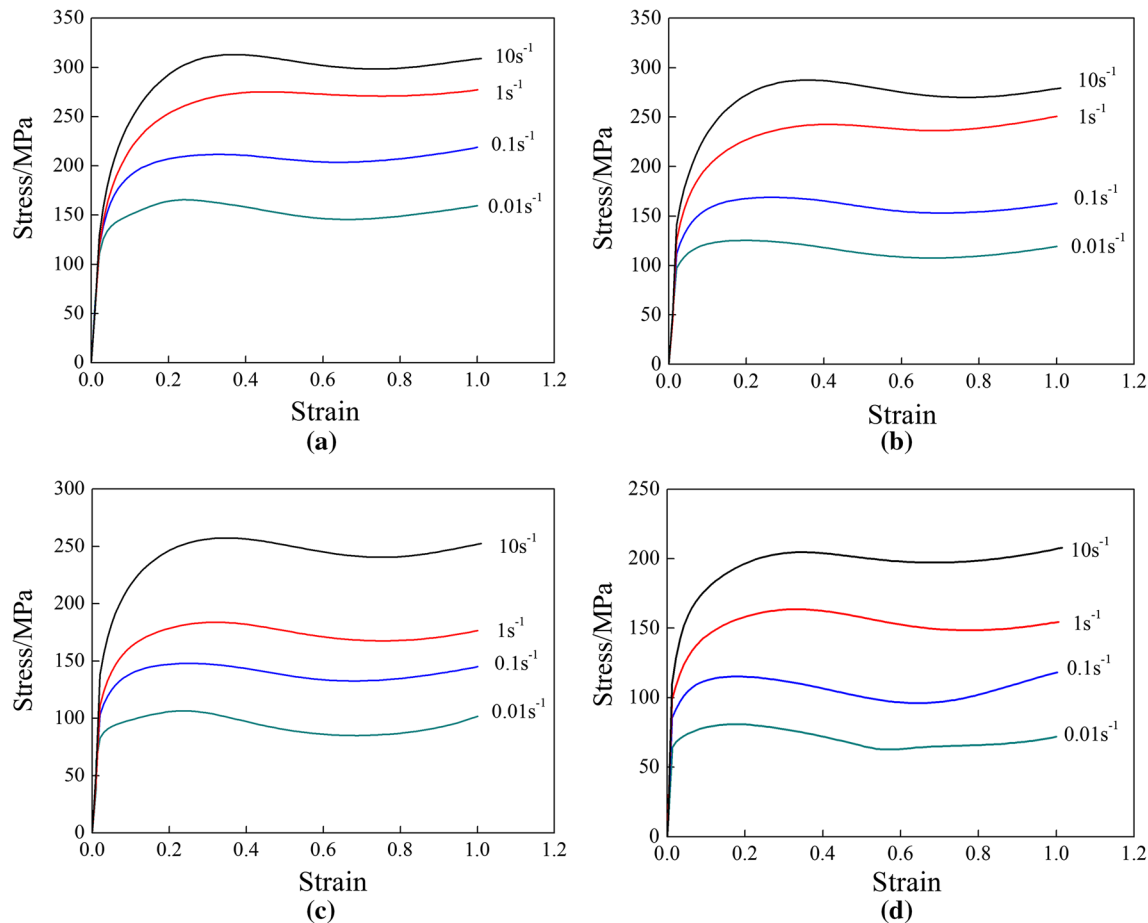


Fig. 2—True stress–true strain curves of the experimental steel at different strain rates with temperatures of (a) 1273 K (1000 °C), (b) 1323 K (1050 °C), (c) 1373 K (1100 °C), and (d) 1423 K (1150 °C).

other hand, a higher strain results in shorter time for growth, and even fewer nucleation sites when the nucleation is not saturated. Therefore, the rapid increase of strain rate leads to either a decreased amount of precipitates with the finer size when the deformation temperature is near the nose temperature for the most rapid precipitation, as suggested by the comparison of Figures 3(a) and (b), or almost no precipitation when the temperature is far away from the nose one (Figures 3(c) and (d)).

2. Recrystallized grains

The recrystallized microstructures after compression tests are shown in Figure 4. Figures 4(a) through (f) confirm that DRX has indeed occurred during all the tests because relatively fine and equiaxed grains resulting from DRX were formed with an average size ranging from a few to 20 micrometers, the latter depending on deformation temperature. The recrystallized grain size increases with either the increase of temperature (Figures 4(b) through (d)) or the decrease of strain rate (Figures 4(e) through (g)), which is within our expectation since higher temperature leads to higher boundary mobility and lower strain rate allows more time for the recrystallized nuclei to grow.^[18,19] A bimodal grain size distribution has also been observed in some samples of

Figure 4. It appears that the grains at the original austenite grain boundaries are obviously finer than those at the interior, which can be clearly seen in the samples deformed with high strain rate and at low temperature in Figures 4(a), (b), and (g). This is a typical necklace structure because DRX starts at the original grain boundaries and new grains are nucleated at the boundaries of the growing grains, leading to a thickening band of recrystallized grains like a necklace. This is often found when the recrystallized grain size is significantly finer than the original grain size, as has been documented.^[19] Since lower temperature and higher strain rate both lead to finer DRXed grain size, Figures 4(a), (b), and (g) show more pronounced bimodal distribution of grain size. In contrast, high temperature and slow strain rate both result in larger DRXed grain size because the recrystallized nuclei can grow larger at high temperature and for longer time; therefore, much fewer fine grains are observed in Figures 4(c) through (f).

It is noted that the increase of strain rate from 1 to 10 s⁻¹ at 1373 K (1100 °C) leads to a clear increase of the fraction of fine grains, as can be seen by the comparison of Figures 4(c) and (g). In contrast, the same increase of strain rate at 1323 K (1050 °C) results in a similar fraction of fine grains, indicated by the

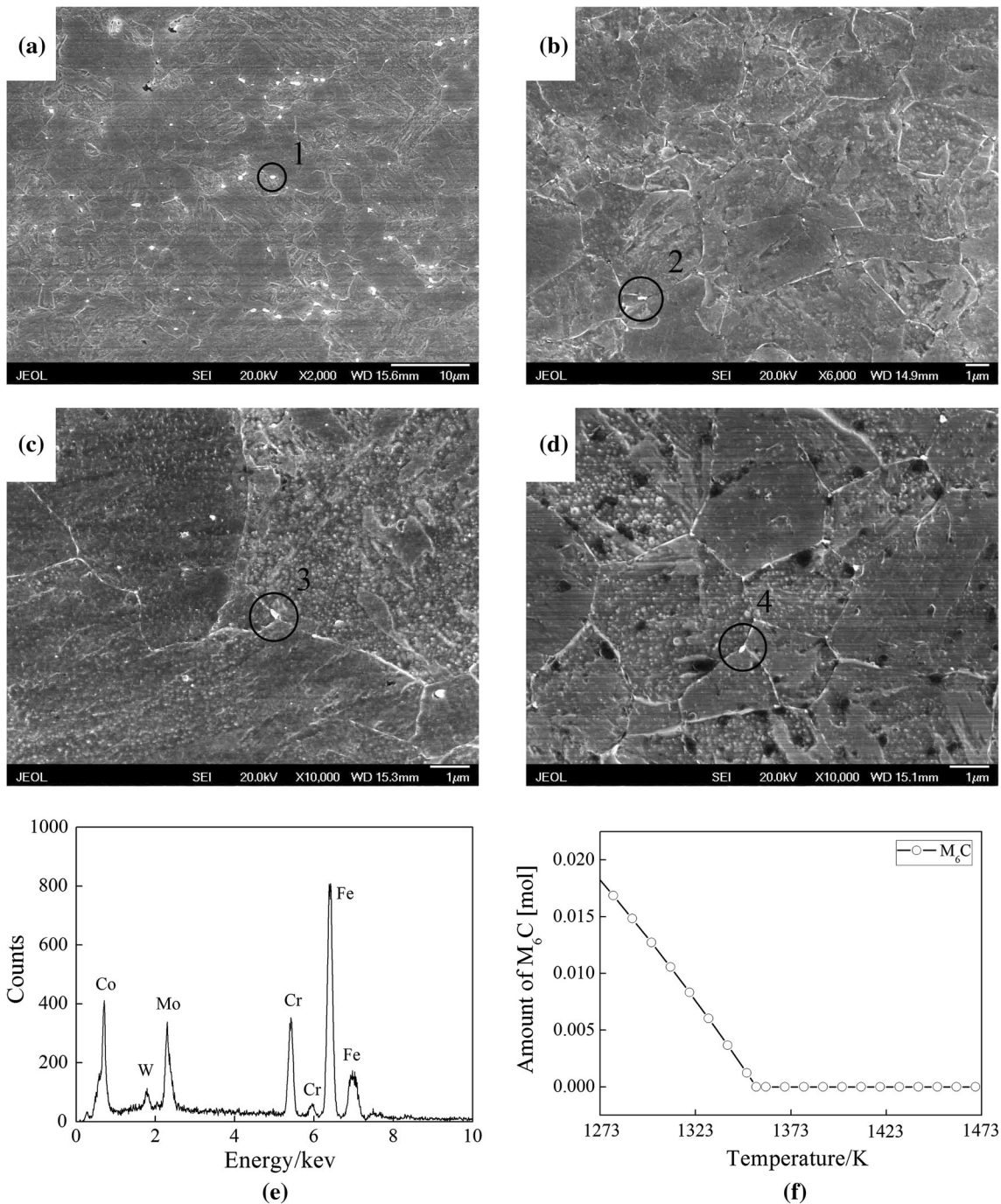


Fig. 3—SEM photos on the precipitates at grain boundaries, indicated by circles, in the specimens deformed (a) at 1273 K (1000 °C) with 0.01 s^{-1} ; (b) at 1273 K (1000 °C) with 10 s^{-1} ; (c) at 1323 K (1050 °C) with 0.01 s^{-1} ; (d) at 1323 K (1050 °C) with 10 s^{-1} ; (e) EDS analysis of particle “1” in (a). (f) The equilibrium amount of M_6C phase precipitates at different temperatures, calculated by ThermoCalc software and TCFE8 database. Compositions of “1”–“4” are 14.43Cr-9.63Co-13.00Mo-1.28W, 14.08Cr-9.29Co-11.02Mo-2.03W, 14.65Cr-9.07Co-12.94Mo-1.15W, and 14.58Cr-10.52Co-13.07Mo-1.27W in weight percentage, respectively.

comparison in Figures 4(a) and (b). Such different microstructural dependence on the strain rate at these two temperatures results from the dependence of dynamic precipitation on temperature. Figure 3 has revealed that dynamic precipitation can occur at 1323 K (1050 °C), which can inhibit the growth of recrystallized

grains, leading to a large fraction of grains having fine sizes even at the low strain rate. Nevertheless, no dynamic precipitation can occur at 1373 K (1100 °C), thereby the low strain rate could allow the recrystallized grains to grow larger, leading to a clear difference of grain size distribution between Figures 4(c) and (g).

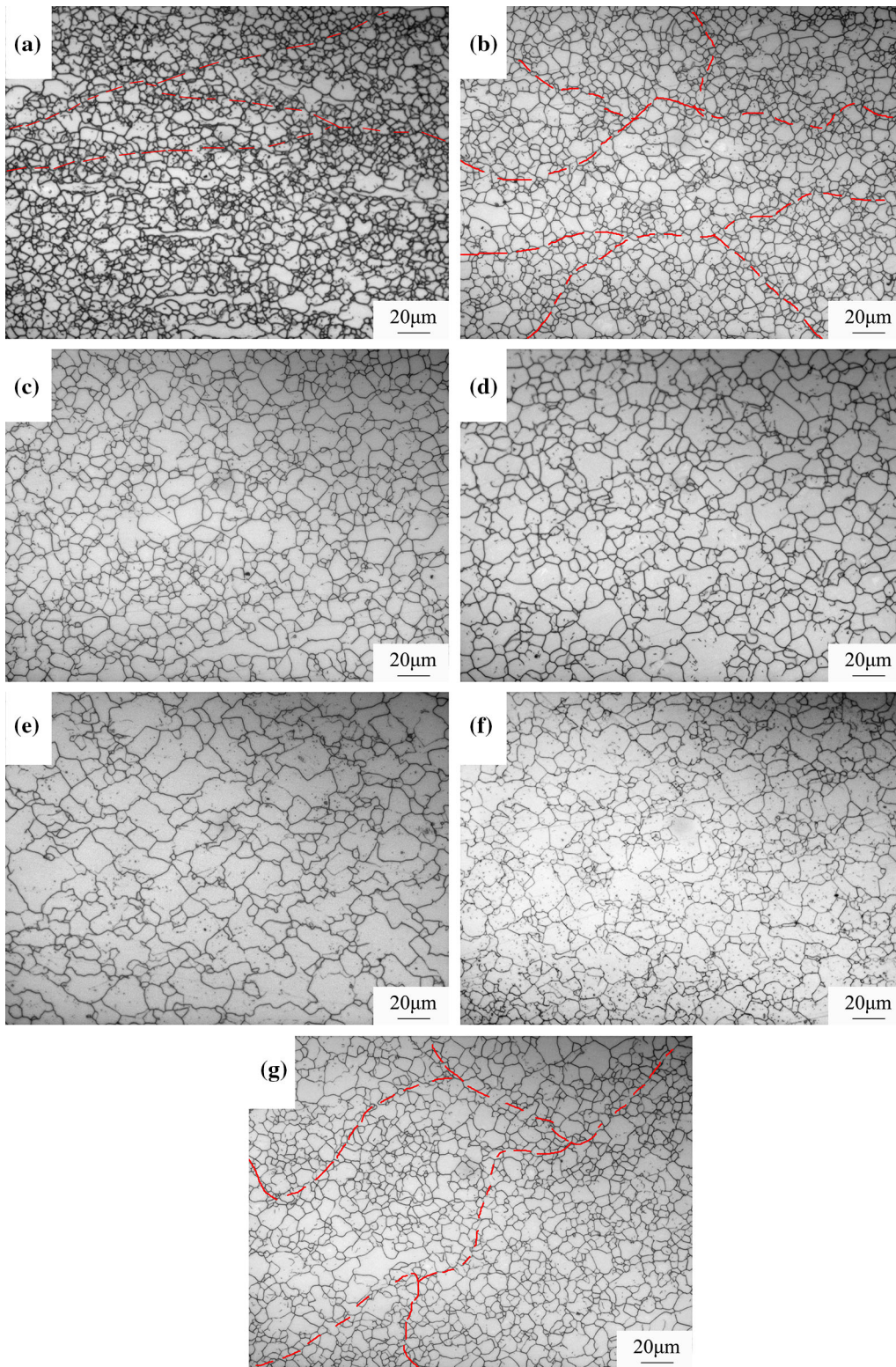


Fig. 4—Typical microstructure of specimens compressed to the true strain of 1.0 at different test conditions: (a) 1323 K (1050 °C), $\dot{\epsilon} = 10 \text{ s}^{-1}$; (b) 1323 K (1050 °C), $\dot{\epsilon} = 1 \text{ s}^{-1}$; (c) 1373 K (1100 °C), $\dot{\epsilon} = 1 \text{ s}^{-1}$; (d) 1423 K (1150 °C), $\dot{\epsilon} = 1 \text{ s}^{-1}$; (e) 1373 K (1100 °C), $\dot{\epsilon} = 0.01 \text{ s}^{-1}$; (f) 1373 K (1100 °C), $\dot{\epsilon} = 0.1 \text{ s}^{-1}$; (g) 1373 K (1100 °C), $\dot{\epsilon} = 10 \text{ s}^{-1}$. Red lines in (a), (b), and (g) indicate the primary austenite grain boundaries (Color figure online).

IV. MODELING AND DISCUSSION

A. Determining the Critical Strain and Stress for DRX

The critical strain and stress for the onset of DRX are important parameters for optimizing the hot working process. First, we need to derive the two types of curves: θ (the work hardening rate of $d\sigma/d\epsilon$) vs σ and $\partial\theta/\partial\sigma$ vs σ , from the flow curves in Figure 2. Figure 5 gives the curves of $-\partial\theta/\partial\sigma$ vs σ . The critical stress, σ_c , is determined by $\partial^2\theta/\partial\sigma^2 = 0$ from Figure 5 by the method shown in Figure 1. It is found that the critical stress is higher at the higher strain rate and the lower temperature, which is within expectation.^[19] Next, the critical strain corresponding to the critical stress can be read from Figure 2.

B. Modeling the Critical/Peak Strain and Stress

The effects of both temperature and strain rate on hot deformation are often described using a single parameter of Zener–Holloman, as given^[20]:

$$Z = \dot{\epsilon} \exp\left(\frac{Q}{RT}\right) \quad [1]$$

where $\dot{\epsilon}$, R , and T are all known as the strain rate (s^{-1}), gas constant ($kJ\ mol^{-1}\ K^{-1}$), and temperature in

Kelvin, respectively, whereas Q is the apparent deformation activation energy and depends on the compositions of steel, which can be derived by the following well-known constitutive equation for the flow stress^[21,22]:

$$\dot{\epsilon} = A [\sinh(\alpha\sigma_p)]^n \exp\left(\frac{-Q}{RT}\right) \quad [2]$$

where σ_p is the peak stress and A and n are constants. Equation [2] can change to:

$$\ln \sinh(\alpha\sigma_p) = -\frac{1}{n} \ln A + \frac{1}{n} \ln(\dot{\epsilon}) + \frac{1}{n} \frac{Q}{RT} \quad [3]$$

At a constant temperature, n is derived by:

$$\frac{1}{n} = \left[\frac{\partial \ln \sinh(\alpha\sigma_p)}{\partial \ln(\dot{\epsilon})}\right]_T \quad [4]$$

Therefore, n is determined as the slope of $\ln \sinh(\alpha\sigma_p)$ vs $\ln(\dot{\epsilon})$ plot. All the linear regressions at different temperatures indeed have similar slopes, as shown in Figure 6. This confirms that Eq. [2] could correctly describe the flow stress in Figure 2. The average of n values at all the test temperatures is then calculated as

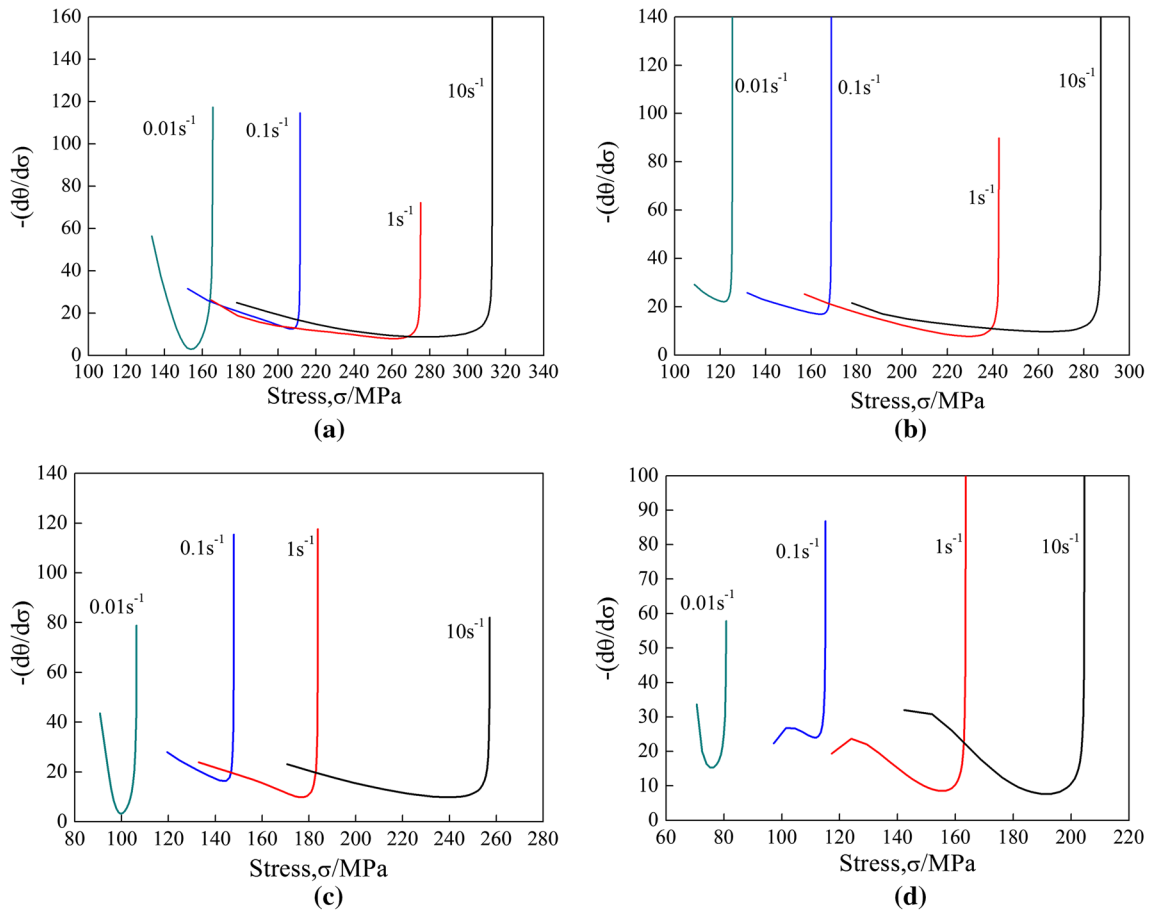


Fig. 5—Determination of the critical stress for DRX from the curves of $-(\partial\theta/\partial\sigma)$ vs σ (a) 1273 K (1000 °C), (b) 1323 K (1050 °C), (c) 1373 K (1100 °C), and (d) 1423 K (1150 °C).

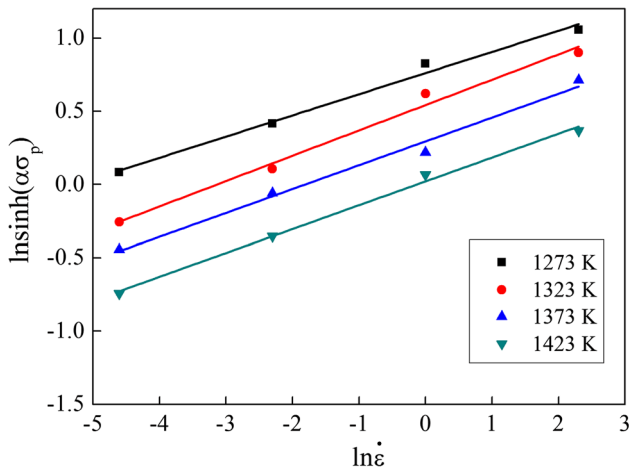


Fig. 6—Relationship between $\ln \sinh(\alpha\sigma_p)$ and $\ln(\dot{\epsilon})$ linearly fitted by Eq. [4].

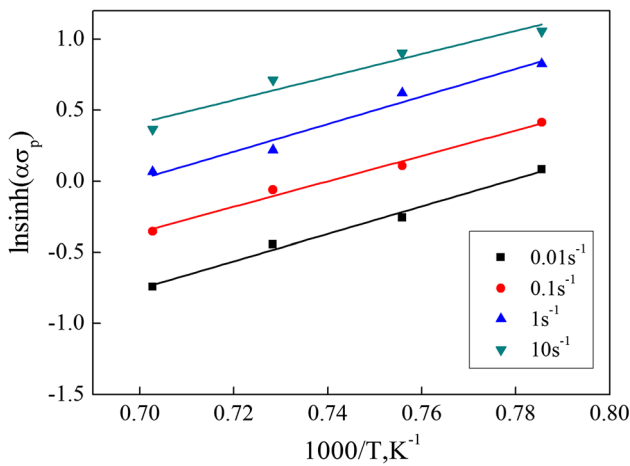


Fig. 7—Relationship between $\ln \sinh(\alpha\sigma_p)$ and $1/T$ linearly fitted by Eq. [5].

6.25, which is used to determine the activation energy, Q , by:

$$Q = nR \left[\frac{\partial \ln \sinh(\alpha\sigma_p)}{\partial (1/T)} \right]_{\dot{\epsilon}} \quad [5]$$

Equation [5] means that Q can be determined as the slope of $\ln \sinh(\alpha\sigma_p)$ vs $1/T$ plot at a constant strain rate. Figure 7 shows that all plots again have similar slopes. The values of apparent activation energy at different strain rates are then averaged as 474 kJ/mol. In comparison with the self-diffusion activation energy of Fe in γ iron, 280 kJ/mol, the typical deformation energy 300 kJ/mol for carbon steels and HSLA steels,^[23] 381 kJ/mol for 300M steel,^[24] the much larger deformation activation energy of studied steel is apparently attributed to its higher contents of Cr, Mo, V, and Co, which leads to higher resisting force during hot deformation.^[25]

When both the critical stress/strain and the peak stress/strain are plotted as the function of Z parameter, they appear to follow a linear relationship on the double logarithm scale, as shown in Figure 8. Therefore, they

can be derived simply from Z by the following equations:

$$\sigma_c = 15.032Z^{0.0244} \quad [6]$$

$$\sigma_p = 1.299Z^{0.0094} \quad [7]$$

$$\epsilon_c = 0.0037Z^{0.0884} \quad [8]$$

$$\epsilon_p = 0.015Z^{0.0804} \quad [9]$$

When the peak and critical strains at both 1273 K and 1323 K (1000 °C and 1050 °C) are plotted as the function of strain rate in Figures 9(a) and (b), respectively, it is found that both critical and peak strains increase with the strain rate until 1 s^{-1} , beyond which a further increase of strain rate from 1 to 10 s^{-1} results in clear decreases of both critical and peak strains. This is unusual since a higher strain rate generally leads to DRX retarded, rather than accelerated. Such an unexpected decrease of critical strain for DRX at a higher strain rate should result from the complicated interaction of DRX and dynamic precipitation during deformation too.^[26] In the range of low strain rates of $0.01\text{--}1 \text{ s}^{-1}$, the deformation time is in the range of 1 to 100 s, which allows a considerable amount of carbides to precipitate during deformation so that DRX is suppressed to various contents depending on the strain rate.^[27] In other words, DRX would start even earlier if no carbide particles precipitated during deformation at the low strain rates. At the highest strain rate of 10 s^{-1} , however, the time for strain-induced precipitation is much shortened to $<0.1 \text{ s}$ so that the quantity of precipitates decreases significantly, causing recrystallization nuclei to grow with little inhibition. Meanwhile, a higher strain rate also leads to a higher work hardening rate and then a larger driving force for DRX. Thus, the critical strain for DRX becomes smaller at the strain rate of 10 s^{-1} . Summarily, strain rate could influence the DRX kinetics of studied steel both directly and indirectly by affecting dynamic precipitation.

In some cases that recrystallization can nucleate at inclusion particles so that the so-called particle-stimulated-nucleation mechanism can operate for enhanced nucleation, which generally happens when a significant strain gradient is developed around a particle with the size more than several micrometers. For an example, Saifei Zhang *et al.*^[11] investigated the role of titanium carbides on microstructural evolution of a fire-resistant titanium alloy Ti-35V-15Cr-0.3Si-0.1C and found that titanium carbides with average particle diameter of $10 \mu\text{m}$ could provide nucleation sites for recrystallization so that recrystallized grains were formed in the vicinity of TiC. Nevertheless, the precipitates with the size of submicrometers generally inhibit recrystallization by pinning the migrating boundaries due to the smaller size, rather than accelerating recrystallization.^[18,19] For

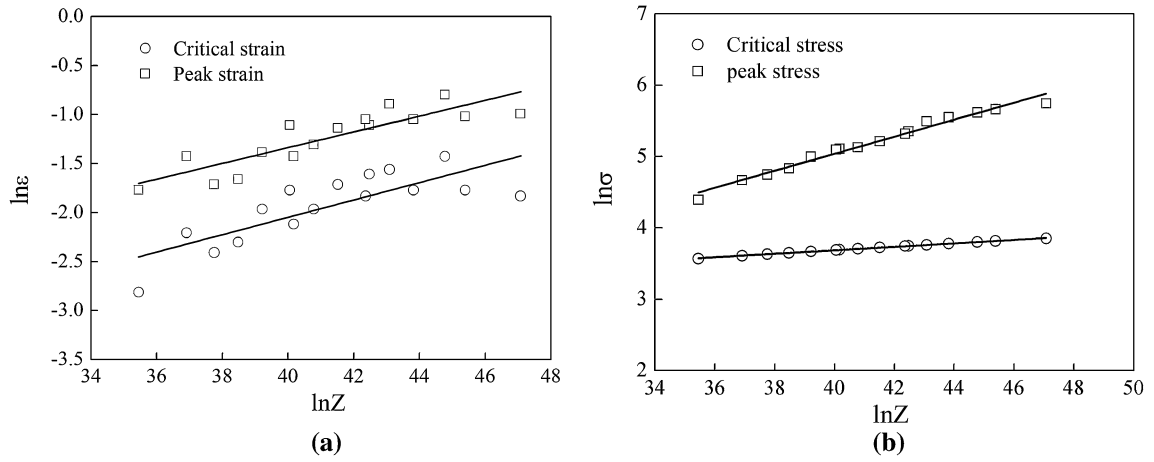


Fig. 8—Dependences of peak/critical strains (a) and stresses (b) on Zener-Holloman parameter according to Eqs. [6] through [9].

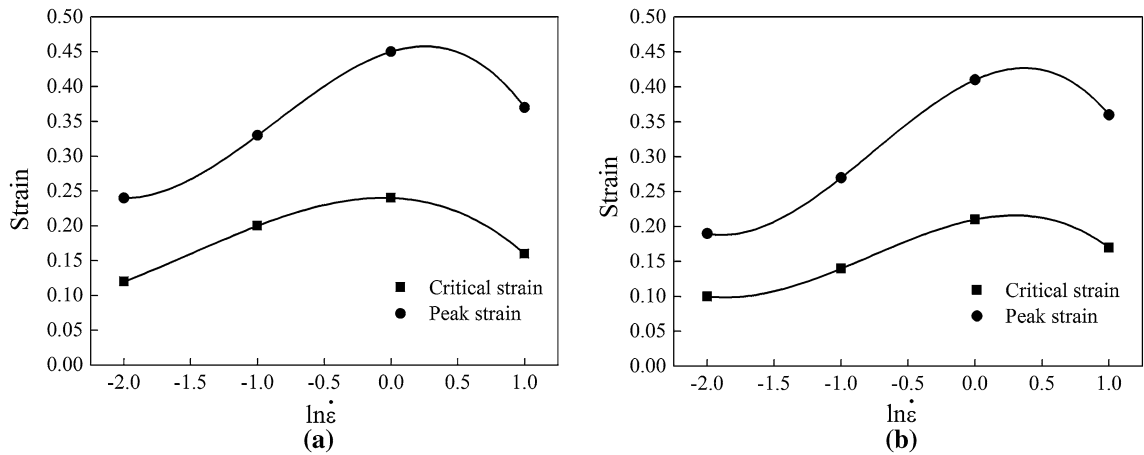


Fig. 9—Dependence of peak/critical strains on the strain rate at 1273 K (1000 °C) (a) and 1323 K (1050 °C) (b).

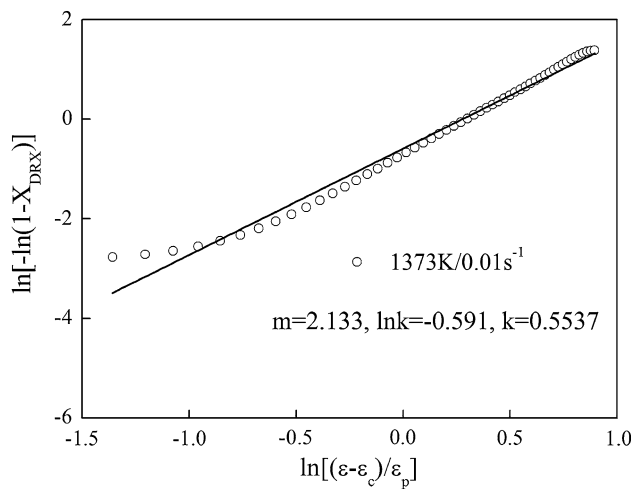


Fig. 10—The relationship between $\ln[-\ln(1 - X_{DRX})]$ and $\ln[(\epsilon - \epsilon_c)/\epsilon_p]$ for the hot deformation at 1373 K (1100 °C) with the strain rate of 0.01 s^{-1} .

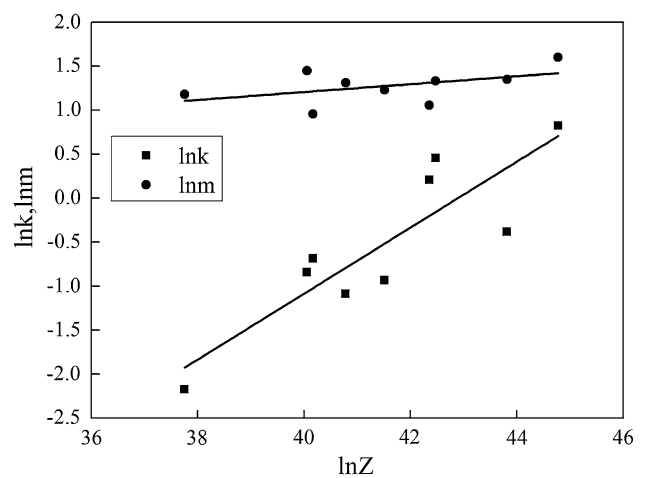


Fig. 11—Dependence of the Avrami modeling parameters for DRX, k and m , on the Zener-Holloman parameter.

an example, Hongyan Wu *et al.*^[28] studied the interaction between DRX and dynamic precipitation of V(C,N) of a Mn-Cu-V weathering steel, and they found that

dynamic precipitation with the sizes from several to tens of nanometers could significantly retard DRX. In our case, it is clear that dynamic precipitation of M_6C

inhibits the DRX due to their relatively fine sizes around several hundreds of nanometers, as shown in Figure 3.

1. Modeling of DRX kinetics

The fraction of DRX is often described using the Avrami model as follows^[24,29]:

$$X_{\text{DRX}} = 1 - \exp \left[-k \left(\frac{\varepsilon - \varepsilon_c}{\varepsilon_p} \right)^m \right] \quad [10]$$

where ε , ε_c , and ε_p are strain, the critical strain for the onset of DRX, and the peak strain, respectively; k and m are both the material constants depending on chemical composition and hot deformation conditions. X_{DRX} , the volume fraction of DRX, can be calculated from the stress-strain curves by^[24,30]:

$$X_{\text{DRX}} = \frac{\sigma_A - \sigma}{\sigma_{S1} - \sigma_S} \quad [11]$$

where σ_A and σ_{S1} are the instantaneous and saturated stress, respectively, if DRV would be the mere softening mechanism, whereas σ_S is the steady flow stress after DRX takes place. All of them are also illustrated in Figure 1 for a better clarification. σ_A during deformation under different conditions is calculated from the following equation based on the mechanism of DRV^[29,31]:

$$\sigma_A = [\sigma_{S1}^2 + (\sigma_0^2 - \sigma_{S1}^2)e^{\Omega\varepsilon}]^{0.5} \quad [12]$$

where σ_0 is the yield stress (MPa). The value of σ_{S1} is derived by linearly extrapolating the plot of θ vs σ to the X axis in the case of DRV as a restoration mechanism, as illustrated in Figure 1(b). Ω is the DRV coefficient, which is dependent on deformation temperature and strain rate. Equation [12] can be changed to:

$$\Omega = \frac{\ln[(\sigma_A^2 - \sigma_{S1}^2)/(\sigma_0^2 - \sigma_{S1}^2)]}{\varepsilon} \quad [13]$$

When Ω and σ_{S1} are both determined, the DRX fraction during deformation can be calculated from the flow stress according to Eq. [11], and then the relationship of $\ln[-\ln(1 - X_{\text{DRX}})]$ vs $\ln[(\varepsilon - \varepsilon_c)/\varepsilon_p]$ is derived. An example is shown Figure 10 for the deformation performed at 1373 K (1100 °C) with the strain rate of 0.01 s^{-1} , which is quite close to the linear relationship. The values of m and k in Eq. [10] are determined as 2.1 and 0.55 from the slope and intercept respectively, leading to the DRX kinetics described by:

$$X_{\text{DRX}} = 0 \quad [14]$$

$$X_{\text{DRX}} = 1 - \exp \left[-0.55 \left(\frac{\varepsilon - \varepsilon_c}{\varepsilon_p} \right)^{2.1} \right] \quad (\varepsilon > \varepsilon_c) \quad [15]$$

Both k and m can be summarized as the function of Z too, as shown in Figure 11, leading to the following equation after the least-square fitting:

$$k = 0.000027Z^{0.24} \quad [16]$$

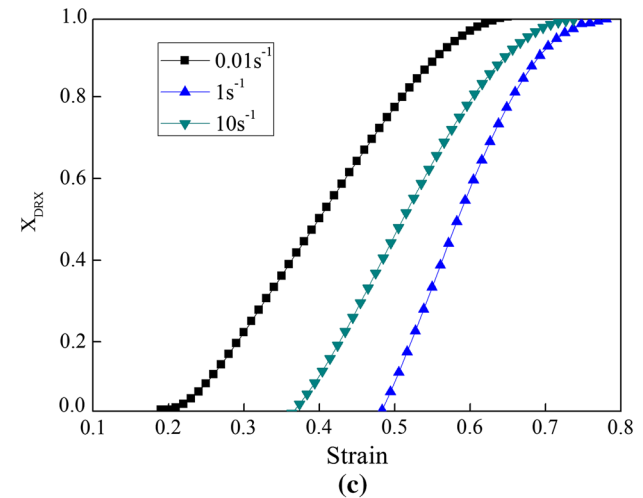
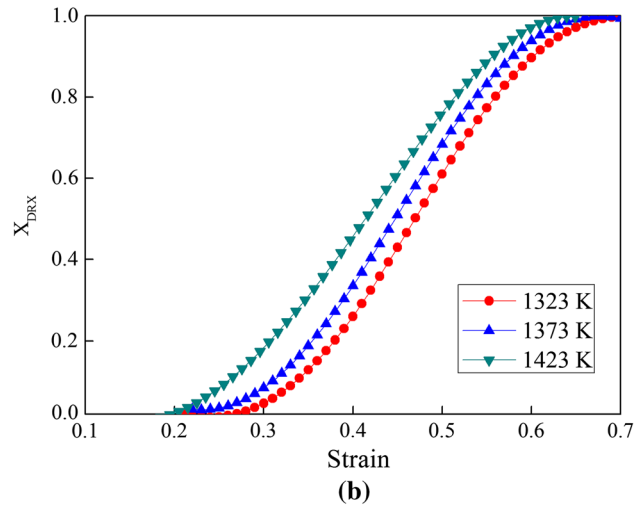
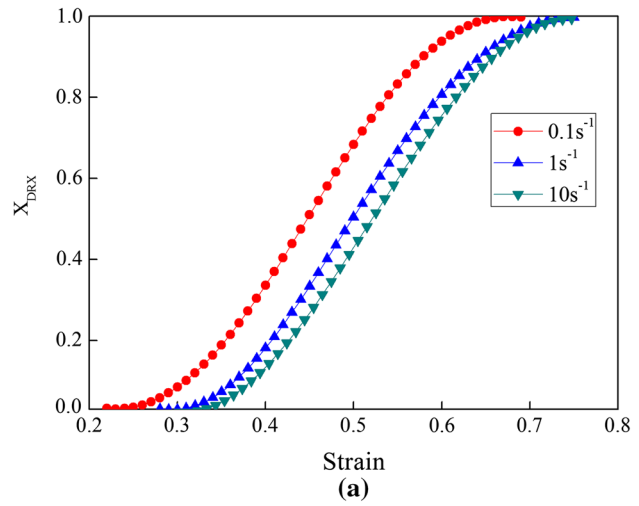


Fig. 12—Calculated fraction of DRX during isothermal compression at 1373 K (1100 °C) (a), 0.1 s^{-1} (b), and 1273 K (1000 °C) (c) with different strain rates.

$$m = 0.56Z^{0.045} \quad [17]$$

Now, the dynamically recrystallized fraction during deformation can be calculated by the combination of

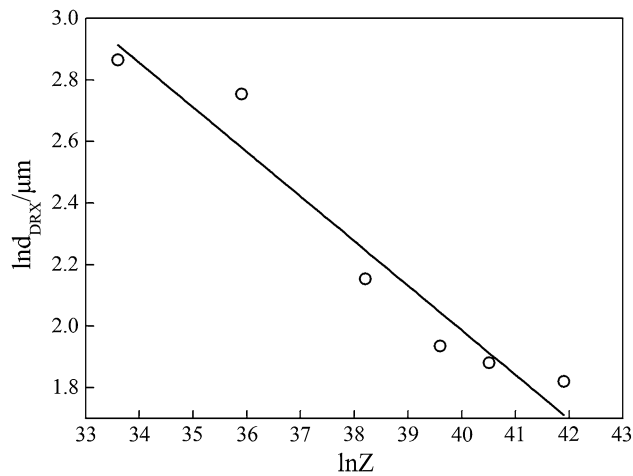


Fig. 13—Relationship between recrystallized grains size, d_{DRX} , and Zener–Holloman parameter.

Eqs. [8] through [10], [16], and [17] just using a single parameter of Z to take both deformation temperature and strain rate into account, as given in Figure 12. The derived model has successfully captured the characteristics of the recrystallization kinetics, such as the critical strain, the “s”-shape kinetic curve, and larger recrystallized fraction at either lower strain rate (Figure 12(a)) or higher temperature (Figure 12(b)). In particular, the simulation on DRX during deformation at 1273 K (1000 °C) also shows that the DRX is unusually accelerated when the strain rate increases from 1 to 10 s^{-1} (Figure 12(c)) due to the stronger suppression of dynamic precipitation during deformation at the higher strain rate, which is consistent with the results in Figure 9.

2. Modeling of the recrystallized grain size

Recrystallized microstructures in Figure 4 suggest that the dynamically recrystallized grain size depends on temperature and strain rate, which is generally described using the Z parameter as^[32,33]:

$$d_{\text{DRX}} = BZ^C \quad [18]$$

where d_{DRX} is the austenite grain size after DRX (μm) and B and C are constants.

It is then known that $\ln d_{\text{DRX}}$ should linearly depend on $\ln Z$, as confirmed in Figure 13. The constants of B and C are then determined as 2398.02 and -0.15 , respectively, by the linear fitting, which leads to the following empirical equation for recrystallized grain size:

$$d_{\text{DRX}} = 2398.02Z^{-0.15} \quad [19]$$

V. CONCLUSIONS

Hot deformation behavior of the UHSSS was investigated at wide ranges of deformation temperatures and strain rates. The following conclusions can be drawn:

- (1) Both the flow stress curves and microstructural examinations suggest that the studied ultra-high-strength heavy alloyed stainless steel could dynamically recrystallize during deformation at the studied temperatures and strain rates.
- (2) Although it is most often reported that both lower temperature and higher strain rate should suppress DRX during hot deformation, we indeed observed an unusual phenomenon in that the increase of strain rate from 1 to 10 s^{-1} at both 1273 K (1000 °C) and 1323 K (1050 °C) could result in an acceleration of DRX rather than in expected suppression. This is attributed to a significant dynamic precipitation of carbides that could occur during deformation at low strain rates below 1353 K (1080 °C) in this heavily alloyed steel.
- (3) A quantitative model for the DRX kinetics has been successfully developed as follows for this steel just using a simple Zener–Holloman parameter that combines the influences of both temperature and strain rate. This model captures all the essential features of DRX as observed experimentally and then can be employed to optimize the hot working process. Moreover, this model has also successfully simulated the unusual acceleration of DRX with the higher strain rate in some cases, which results from the complicated interaction of dynamic precipitation and DRX:

$$\left\{ \begin{array}{l} X_{\text{DRX}} = 1 - \exp \left[k \left(\frac{\varepsilon - \varepsilon_c}{\varepsilon_p} \right)^m \right] \quad (\varepsilon > \varepsilon_c) \\ k = 0.000027Z^{0.24} \\ m = 0.56Z^{0.045} \\ \varepsilon_c = 0.0037Z^{0.0884} \\ \varepsilon_p = 0.015Z^{0.0804} \end{array} \right.$$

REFERENCES

1. Z.B. Liu, Z.Y. Yang, Q.L. Yong, J.X. Liang, Y.Q. Sun, W.H. Li, and C.Y. Song: *J. Iron Steel Res.*, 2008, vol. 5, pp. 27–32.
2. Z.Y. Yang, Z.B. Liu, J.X. Liang, Y.Q. Sun, and W.H. Li: *Trans. Mater. Heat Treat.*, 2008, vol. 29, pp. 1–7.
3. Z. Guo, W. Sha, and D. Vaumousse: *Acta Mater.*, 2003, vol. 5, pp. 101–16.
4. Y.C. Li, W. Yan, J.D. Cotton, G.J. Ryan, Y.F. Shen, W. Wang, Y.Y. Shan, and K. Yang: *Mater. Des.*, 2015, vol. 82, pp. 56–63.
5. G.L. Ji, F.G. Li, Q.H. Li, H.Q. Li, and Z. Li: *Mater. Sci. Eng. A*, 2010, vol. 527, pp. 2350–55.
6. D.M. Li, R.P. Gangloff, and J.R. Scully: *Metall. Trans. A*, 2004, vol. 35, pp. 849–64.
7. J. Wang, H. Xiao, H.B. Xie, X.M. Xu, and Y.N. Gao: *Mater. Sci. Eng. A*, 2012, vol. 539, pp. 294–300.
8. M.A. Khafri and F. Adhami: *Mater. Sci. Eng. A*, 2010, vol. 527, pp. 1052–57.
9. S. Mandal, A.K. Bhaduri, and V.S. Sarma: *Metall. Trans. A*, 2012, vol. 43, pp. 2056–68.
10. M.C. Mataya, C.A. Perkins, S.W. Thompson, and D.K. Matlock: *Metall. Trans. A*, 1996, vol. 27, pp. 1251–66.
11. H. Mirzadeh and A. Najafzadeh: *Mater. Des.*, 2010, vol. 31, pp. 1174–79.

12. T. Xia, C.G. Yang, M.B. Shahzad, and K. Yang: *Mater. Des.*, 2015, vol. 87, pp. 303–12.
13. G.R. Ebrahimia, H. Keshmirib, A.R. Maldadb, and A. Momenic: *J. Mater. Sci. Technol.*, 2012, vol. 28, pp. 467–73.
14. E.I. Poliak and J.J. Jonas: *Acta Mater.*, 1996, vol. 44, pp. 127–36.
15. H. Mirzadeha, J.M. Cabrera, and A. Najafizadeh: *Acta Mater.*, 2011, vol. 59, pp. 6441–48.
16. M.E. Wahabi, J.M. Cabrera, and J.M. Prado: *Mater. Sci. Eng. A.*, 2003, vol. 343, pp. 116–25.
17. Y. Han, G.W. Liu, D.N. Zou, R. Liu, and G.J. Qiao: *Mater. Sci. Eng. A.*, 2013, vol. 565, pp. 342–50.
18. F.J. Humphreys and M. Hatherly: *Recrystallization and Related Annealing Phenomena*, second ednd ed., Pergamon, Tarrytown, 2004, pp. 417–18.
19. S.F. Medina and C.A. Hernandez: *Acta Mater.*, 1996, vol. 44, pp. 137–48.
20. C.M. Sellars and W.J.McG. Tegart: *Int. Mater. Rev.*, 1971, vol. 17, pp. 1–24.
21. J.B. Jia, K.F. Zhang, and Z. Lu: *Mater. Sci. Eng. A.*, 2014, vol. 607, pp. 630–39.
22. H.J. McQueen and N.D. Ryan: *Mater. Sci. Eng. A.*, 2002, vol. 1, pp. 43–63.
23. Y.G. Liu, M.Q. Li, and J. Luo: *Mater. Sci. Eng. A.*, 2013, vol. 574, pp. 1–8.
24. E.X. Pu, W.J. Zheng, J.Z. Xiang, Z.G. Song, and J. Li: *Mater. Sci. Eng. A.*, 2014, vol. 598, pp. 174–82.
25. G.R. Ebrahimia, H. Keshmiria, A. Momenib, and M. Mazinanic: *Mater. Sci. Eng. A.*, 2011, vol. 528, pp. 7488–93.
26. A. Momeni, K. Dehghani, H. Keshmiri, and G.R. Ebrahimi: *Mater. Sci. Eng. A.*, 2010, vol. 527, pp. 1605–11.
27. S.F. Zhang, W.D. Zeng, D.D. Zhou, Y.J. Lai, and Q.Y. Zhao: *Mater. Lett.*, 2015, vol. 166, pp. 317–20.
28. H.Y. Wu, X.H. Liu, and L.X. Du: *J. Mater. Sci. Technol.*, 2011, vol. 27, pp. 1131–38.
29. C. Zhang, L.W. Zhang, W.F. Shen, C.R. Liu, Y.N. Xia, and R.Q. Li: *Mater. Des.*, 2015, vol. 90, pp. 804–14.
30. A. Laasraoui and J.J. Jonas: *Metall. Trans. A.*, 1991, vol. 22, pp. 1545–58.
31. J.J. Jonas, X. Queleynec, L. Jiang, and É. Martin: *Acta Mater.*, 2009, vol. 57, pp. 2748–56.
32. H.Y. Kim, W.H. Sohn, and S.H. Hong: *Mater. Sci. Eng. A.*, 1998, vol. 251, pp. 216–25.
33. F. Chen, Z.S. Cui, and S.J. Chen: *Mater. Sci. Eng. A.*, 2011, vol. 528, pp. 5073–80.